applied sciences

Article

Auto-Detection of Hidden Corrosion in an Aircraft Structure by Electromagnetic Testing: A Machine-Learning Approach

Minhhuy Le [1,2], Van Su Luong [1,2], Dang Khoa Nguyen [1,2], Dang-Khanh Le [3] and Jinyi Lee [4,5,6,*]

1 Faculty of Electrical and Electronic Engineering, Phenikaa University, Hanoi 12116, Vietnam; huy.leminh@phenikaa-uni.edu.vn (M.L.); su.luongvan@phenikaa-uni.edu.vn (V.S.L.); khoa.nguyendang@phenikaa-uni.edu.vn (D.K.N.)
2 Intelligent Communication System Laboratory (ICSLab), Phenikaa University, Hanoi 12116, Vietnam
3 Faculty of Marine Engineering, Vietnam Maritime University, Haiphong 180000, Vietnam; ledangkhanh@vimaru.edu.vn
4 IT-Based Real-Time NDT Center, Chosun University, Gwangju 61452, Korea
5 Department of Electronics Engineering, Chosun University, Gwangju 61452, Korea
6 Interdisciplinary Program in IT-Bio Convergence System, Chosun University, Gwangju 61452, Korea
* Correspondence: jinyilee@chosun.ac.kr

Abstract: An aircraft is a multilayer structure that is assembled by rivets. Under extreme working conditions, corrosion appears and quickly propagates at the rivet sites of the layers; thus, it threads the integrity and safety of the aircraft. Corrosion usually occurs at the hidden layer around the rivet, making it difficult to detect. This paper proposes a machine learning approach incorporating an electromagnetic testing system to detect the hidden corrosion at the riveting site effectively. Several machine learning methods will be investigated for the detection of different sizes and locations of corrosion. The training strategy of the machine-learning models on the small numbers of data will also be investigated. The result shows that the proposed approach could effectively detect 89.48% of the hidden corrosion having from 2.8 to 195.4 mm^3 with only 20% of training data and could be increased to 99.0% with 60–80% of the training data.

Keywords: electromagnetic testing; rivet corrosion; aircraft intake; hall sensor array; machine learning

Citation: Le, M.; Luong, V.S.; Nguyen, D.K.; Le, D.-K.; Lee, J. Auto-Detection of Hidden Corrosion in an Aircraft Structure by Electromagnetic Testing: A Machine-Learning Approach. *Appl. Sci.* **2022**, *12*, 5175. https://doi.org/10.3390/app12105175

Academic Editors: Barbara Grochowalska and Grzegorz Psuj

Received: 29 April 2022
Accepted: 18 May 2022
Published: 20 May 2022

1. Introduction

The aircraft intake and skins of aircraft bodies are constructed by multilayers of aluminum alloys assembled by riveting. Aircraft work under extreme conditions such as high pressure, large changing temperature, and repeated load. Salinity and moisture in the environment could attach and accumulate to the riveting site and quickly propagate corrosion in the riveting area. Most corrosion was observed at the gap between the layers, on the hidden layer, and this is the original reason for aircraft accidents in history [1–3]. It is required to detect the corrosion at an early stage for the safety and integrity of the aircraft structure.

Nondestructive testing (NDT) is a common methodology for detecting corrosion in aircraft. Due to the location of corrosion in the hidden area under the first layer, it is impossible to detect the corrosion by visual testing. Ultrasonic testing (UT) is a powerful method for detecting corrosion on the surface or hidden inside the material. However, UT requires continuous mediums for ultrasonic wave propagation and reflection [4,5]. Thus, the UT method could not be applied in the multilayer structure of air intake where the air gap exists between the layers. The electromagnetic acoustic transducer (EMAT) system is the combination technique of the UT and eddy current testing (ECT). In the EMAT system, an ECT module generates a high-frequency eddy current into the materials and produces ultrasonic sound caused by the vibration; then, a UT sensor is used to measure the echo [6]. However, the air gap between the layers makes it hard for the echo from the corrosion to propagate to the UT sensor. Thus, it is not feasible to use EMAT. Instead, electromagnetic testing is a good candidate because the electromagnetic field could penetrate through the air gap and the layers. Magneto-optical imager (MOI) systems have been successfully developed for the inspection of corrosion in airplanes [7,8]. An MOI system, including a magnetic source for generating a magnetic field into the multilayers and a large magneto-optical films (e.g., bismuth-doped iron garnet), is used to measure the rotation angle of the optical beam while passes through the magnetic field. Thus, the hidden corrosion in the multilayer could be detected. However, the MOI signal has a low resolution (1 bit: black (0) or white (1) color); thus, it is limited in the quantitative evaluation of the corrosion in the later analysis. In addition, the size of MOI film is large and difficult to use in the complex curve surface in the air intake.

ECT is an alternating electromagnetic field testing in which sensing coils or magnetic sensors are used to measure the changes in the magnetic field produced by the corrosion. Thus, the corrosion could be detected and quantitatively evaluated its size. Several eddy current testing (ECT) methods have been proposed to detect the hidden corrosion in the multilayer structure [8–15]. The ECT methods could be classified based on the excitation source of the magnetic field, which are single-frequency (SF-ECT), multiple-frequency (MF-ECT), and pulse (P-ECT) signals. SF-ECT uses a single frequency of sinusoidal current supplying to an exciting coil to produce an electromagnetic field [9]. The sensing element could simply be a coil, Hall sensor, or giant magnetoresistance (GMR) sensor. In the MF-ECT system, the sensing element could be the same as used in the SF-ECT, but a multiple frequency current was supplied to the exciting coil [10,11]. With multiple frequencies, the eddy current could be penetrated at different depths, and thus, multiple characteristics of the measured signal could be obtained. So, the MF-ECT could better detect the hidden corrosion than the SF-ECT does. P-ECT uses a pulse wave shape for the exciting signal, which is a frequency-rich driven signal; thus, rich characteristics of the measured signal could be obtained [12–25]. It helps to detect hidden corrosion better. However, the signal is more complicated, and it is not easy to recognize the corrosion because of the effect of the rivet and fastener hole, so the signal of corrosion could be masked in the rivet and fastener hold signal.

Machine learning has been used to analyze the ECT signal for detection and classification of the hidden corrosion in the multilayers structure. Principal component analysis (PCA) was used to detect notches at the fastener hole in the P-ECT probe [10]. The P-ECT probe has eight pick-up coils around an exciting coil, which makes it possible to detect all the positions of the notches around the fastener hole. In another study [17], surface and subsurface defects were classified by a combination of the PCA features, spectral characteristics features, peak value, and peak time features. PCA was applied to extract features of the PECT signal of the defects at the upper layer and deeper layer, then a random forest (RF) classifier was used to classify the defects according to their localization [18]. A convolutional neural network (CNN) has been proposed to classify defects in different layers and simultaneously evaluate defect depth [19]. Additionally, a support vector machine (SVM) method has been used to classify the internal states of the multilayer structure with the combination of lift-off features and PCA features [20]. With the machine learning techniques, defects in the multilayer structure could be accurately classified. However, the ECT probes contain a sensing element [17–20] or a few sensing elements (e.g., eight pick-up coils [16]), which make the inspection operation complicated and time-consuming while scanning. In addition, the use of pick-up coils limits the spatial resolution of the sensor probe due to the size of the coil.

Magnetic sensor arrays were developed [21–24], which have multiple magnetic sensor elements arrayed in a high spatial resolution. The use of multiple magnetic sensors (e.g., Hall sensors [21,22] and GMR sensors [23,24]) in the ECT probes helps to measure the higher quality of the corrosion in the multilayer structures. However, the electromagnetic field induced by the rivet and fastener hole was observed to be very large compared to the field induced by corrosion; thus, it is difficult to detect corrosion [21,22]. In addition, the special design of the magnetic sensor probe uses only a single large magnetic source for the sensor array; thus, the measured magnetic field distribution around the rivet and corrosion has a strong correlation. Two-layer specimens similar to the skin of the aircraft intake were fabricated and tested with and without artificial corrosion. The hidden corrosion in the second layer at different locations around the fastener holes was detected and classified according to its location. The previous study used handcraft features, "Sum of area" (SoA) [22], for the detection of the corrosion. Four areas around the rivet were selected, summed, and compared with thresholds. This method could detect the smallest corrosion with a volume of 46.35 mm^3 with 90% probability of detection (POD) and 95% confidence. However, the SoA features were not considered the correlation of the signals at the corrosion area and rivet site. Thus, in this paper, data-driven learning features will be extracted by principal component analysis (PCA) on the correlation of all the sensor signals. Then, machine learning techniques will be applied to the learning features to detect and classify the hidden corrosion in the multilayer structure. The machine-learning models will be trained on different ranges of corrosion volume and a different number of corrosion samples to find an effective training dataset with fewer data (e.g., 20% on a small corrosion volume from 15.0 to 25.4 mm^3). The results could be helpful for further design of experiments, especially in the electromagnetic testing where the data sample is limited. The improvement of POD will be also obtained and compared with the previous study.

2. Electromagnetic Testing Principle

A general principle of the proposed method is shown in Figure 1. The system has three main blocks: an electromagnetic testing probe, signal processing unit, and auto-detection algorithm based on machine learning techniques. The sensor probe has a multiple C-slice core shape made of silicon steel with a copper coil supplied by an alternating current to produce an alternating magnetic field (B_o) according to Ampère's law. An eddy current in the multilayer is then produced according to Faraday's law. The eddy current penetrates into the specimen according to the skin effect, which is inversely proportional to the exciting frequency. The strength of the eddy current decreases exponentially with the depth from the surface of the specimen. Thus, the exciting frequency is calculated so that the eddy current can penetrate the hidden corrosion depth. The eddy current is distorted by the presence of the rivet and hidden corrosion and produces the secondary magnetic field (B_z). The B_z could be measured by the Hall sensor array at the center of the C-core. The measured magnetic field B_z is in the vertical direction as the sensitive direction of the Hall sensors. The alternating output voltage of the Hall sensor array is low-pass filtered (LPF) and amplified before converting to DC voltage by the root-mean-square (RMS) circuits. The number of LPF, amplifier and RMS circuits is the same as the number of Hall sensor elements for simultaneous signal processing. The signal is then digitalized by a data acquisition device (National Instrument DAQ) and transferred to a computer.

Support, f, δ, μ, α, and B_{zo} are the exciting frequency of the coil, electrical conductivity, permeability of specimen, phase shift of magnetic field, and am amplitude of the total magnetic field in the vertical direction. The eddy current strength and skin depth are calculated by Equation (1). The output voltage of the Hall sensor element is proportional to the magnetic field as described in Equation (2), where k and I are the constant factor and supplied current of the Hall sensor. The measured RMS voltage is then to the magnetic field B_{zo}, as calculated by Equation (3).

$$J_d = J_{surf} e^{-d/\delta} \quad \text{with} \quad \delta = 1/\sqrt{\pi f \mu \sigma} \tag{1}$$

$$V_H(t) = k \times I \times B_Z(t) = k \times I \times B_{z0} Sin(2\pi f t + \alpha) \tag{2}$$

$$V_{RMS} = \sqrt{\frac{1}{T}\int_0^T [V_Z(t)]^2 dt} \approx k \times I \times \frac{1}{\sqrt{2}} B_{z0} \tag{3}$$

where f is the exciting frequency [Hz]; δ is the electrical conductivity of specimen [m/S]; μ is the absolute permeability of specimen [H/m]; J_{surf} and J_d are the eddy current on the surface and at depth d from the surface of specimen [A/m], respectively; δ is the skin depth [m]; B_{z0} is the amplitude of magnetic field in vertical direction [T]; k is the Hall constant [V.(A.mT)$^{-1}$]; V_H and I are Hall output voltage and current supply [V], [A]; α is the phase shift of magnetic field [rad]; and, V_{RMS} is the root-mean-square of the Hall output voltage [V].

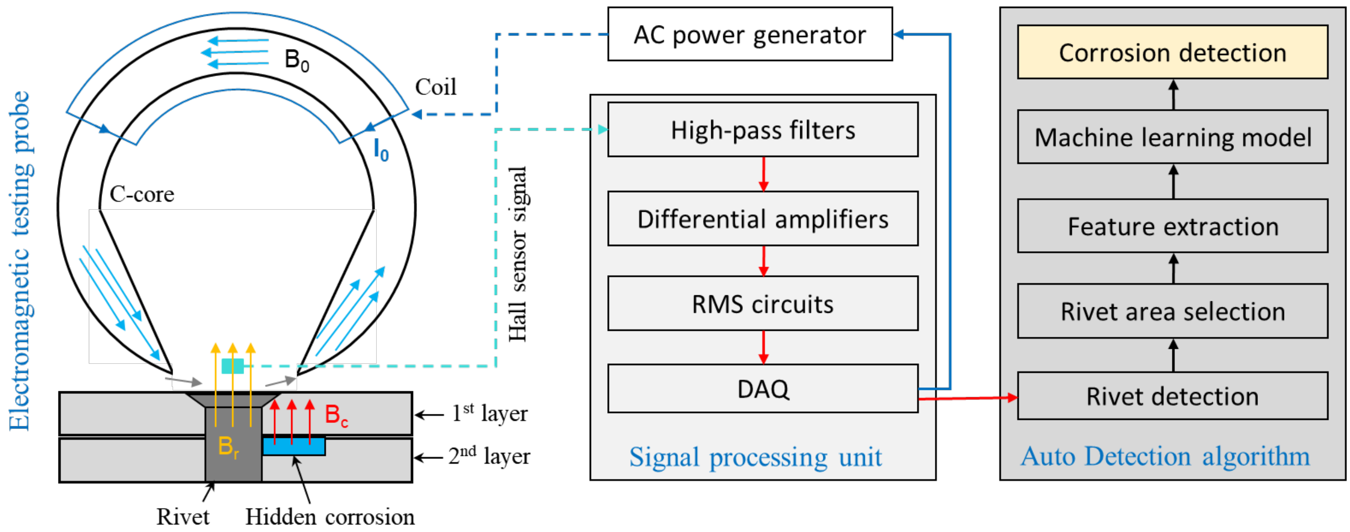

Figure 1. Principle of the electromagnetic testing system with the integration of machine learning techniques.

It is noted that the total magnetic field B_{zo} is the superposition of the magnetic field from the primary magnetic field (B_o), eddy current of the multilayers (B_m), distorted eddy current by the rivet (B_r), and corrosion (B_c). However, the B_o and B_m could be assumed constant, and the variations of B_{ro} only depend on the superposition of the B_r and B_c. The magnetic field from corrosion is usually very small compared to the rivet ($B_c < B_r$); thus, detecting the corrosion is difficult. Another issue is that the amount of data for training the machine-learning model is low due to the expensive and time-consuming experiments. Due to the large signal of the rivet, the rivet center could be detected [22], and only an area of data around the rivet is selected as the input for the feature extraction module to reduce abundant data in the no-corrosion area. Principal component analysis (PCA) was used to auto extraction of features and reduce the data dimension. The extracted principal component features will be used for training machine-learning models.

3. Data Preparation

3.1. Experimental Setup

Figure 2 shows the experimental setup of the electromagnetic testing system. The signal processing circuit and sensor probe were attached to an XY-stage scanner to scan entire rivets on the specimen. The XY-stage scanner triggers the acquisition device with respect to the scan step of 0.5 mm at a scan speed of 32 mm/s. The lift-off was maintained at 0.3 mm during scanning using four wheels on the sensor probe. The Hall sensor array has 64 InSb elements arrayed at an interval of 0.52 mm. The magnetic source was excited with a current amplitude of 0.1 A and a frequency of 900 Hz. The skin depth was about 3.2 mm, enough to penetrate the two layers specimen (each layer has a 1.27 mm thickness). The output voltage of the Hall sensors was high-pass filtered at 284 Hz and amplified at 60 dB. The numbers of high-pass filters, amplifiers, and RMS circuits are the same as the number of Hall sensors, 64. The signal is then digitalized with a 2.441 mV/bit resolution by a NI-PCI 6071E device [21,22]. The detailed specifications of the components are shown in Table 1.

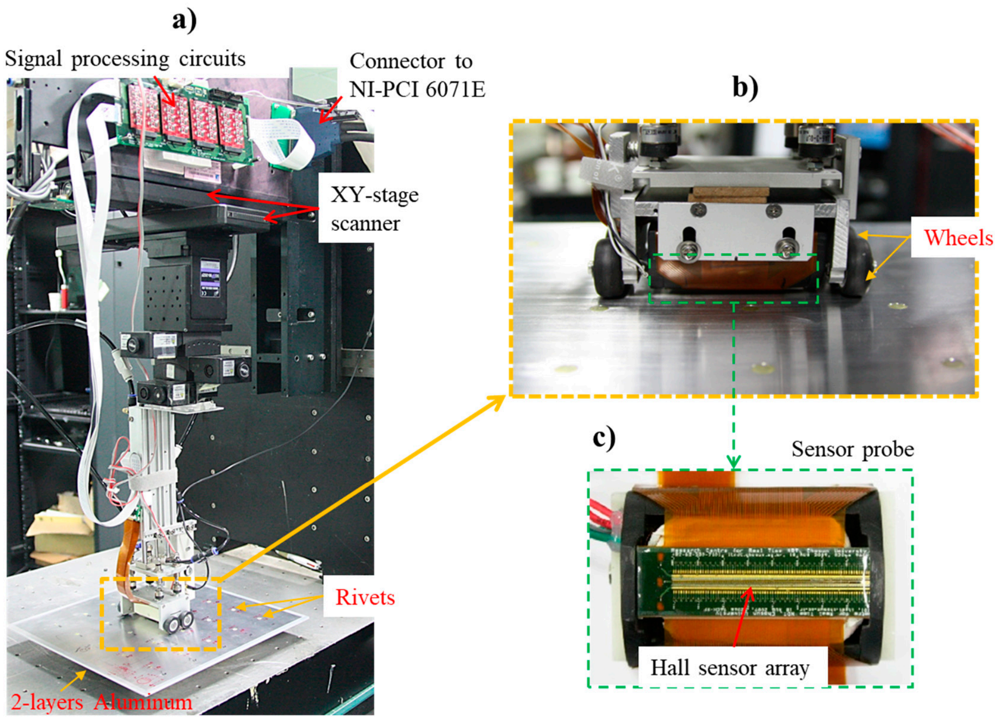

Figure 2. Experimental setup of electromagnetic testing on a two-layer aluminum specimen: (**a**) sensor probe attached to XY-stage scanner with signal processing circuits, (**b**) sensor probe on a specimen, and (**c**) Hall sensor array on the sensor probe.

Table 1. Properties of components in the electromagnetic testing system.

	Components	Properties
Sensor probe	*Core*	Thin slices: 10 Material: Silicon steel Size: 13 × 20 × 50 mm (inner dia., outer dia., height)
	Coil	Turns: 1220 Copper wire: 0.2 mm diameter Current supply: 0.1 A Frequency: 900 Hz
	Hall sensor array	Hall elements: 64 InSb Element interval: 0.52 mm Length: 33.28 mm
Signal processing	*High-pass filter*	Type: RC Cut-off frequency: 284 Hz To remove low-frequency noise signal
	Amplifier	Differential type: INA128 No. of elements: 64 Gain: 60 dB
	RMS circuits	AD8436 chipset No. of elements: 64
	ADC	Device: NI-PCI 6071E Channels: 64 Resolutions: 12-bit, 2.441 mV/bit Sampling rate: 1.25 MS/s Sampling trigger at each 0.5 mm from XY-stage scanner
Specimen & Corrosion	*Specimen*	Two aluminum alloy layers (Al 2024) Size: 300 × 300 × 1.27 mm No. of Rivets: 25 (AN426 AD-5-6, Air Force and Navy standard)
	Artificial Corrosion	No. of corrosion: 25 Diameters: 6, 8, 10, 12, 14 mm Depths: 0.1, 0.3, 0.6, 0.9, 1.27 mm (Through) Volumes: 2.8~195.4 mm^3 On rivet sites of the second layer

There are two specimens with and without artificial hidden corrosion. Each specimen has two aluminum (Al 2024) layers and 25 rivets. The rivets are commercial aircraft countersunk rivets (AN 426 AD-5-6) with diameters of the head and shank of 5.85 and 3.95 mm, respectively. Artificial corrosion was fabricated on the riveting site of the upside surface of the second layer with diameters of 6.0, 8.0, 10.0, 12.0, 14.0 mm and depths of 0.1, 0.3, 0.6, 0.9, 1.27 mm. Thus, there are 25 distinguish volumes of corrosion. The sketch of the rivet with hidden corrosion on the second layer is shown in Figure 3. During the experiment, the corrosive specimen was rotated at 0°, 90°, 180°, and 270° such that the corrosion was on the four sides of the scanning direction, which are forward, backward, left, and right side. Thus, it is needed to detect corrosion and determine the location of the corrosion. The no-corrosion specimen was rotated at 0° and 90° only. With each rotation, the experiment was repeated four times, and each scan could cover three rivets. Thus, in total, there are 720 scanned images of rivets, including 480 rivets with corrosion and 240 rivets without corrosion [22].

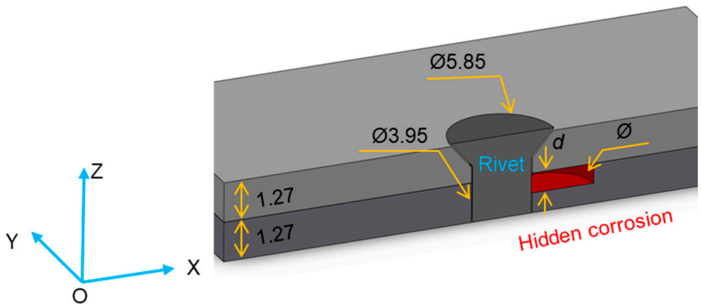

Figure 3. Two-layer specimen with a rivet with hidden corrosion on the second layer.

3.2. Data Preparation

As described in the previous section, each scan of the sensor probe could cover a few rivets according to the scan length of the scanner (e.g., three rivets); therefore, it is necessary to separate each rivet data before detection of corrosion. It is observed that the rivet signal has high intensity, so it is easy to detect and separate the rivet by the peak detection algorithm [22]. However, the rivet is not always at the center of the scanned image, and the total number of images is only 720. Thus, random shifting of the magnetic image window around the rivet increases the number of magnetic images. The magnetic image window was set with a size of 56 × 80 pixels with respect to 30 × 40 mm (in sensor length × scan direction), which is shorter than the sensor length (64 pixels) but enough to cover the entire the rivet. Finally, there are 18,000 magnetic images in the dataset. For performing feature extraction by PCA and machine learning algorithm, the dataset was transformed into two dimensions, which has a size of 18,000 × 4480. There are five classes of the rivet, which have no corrosion, forward, backward, left, and right corrosion.

Figure 4 shows samples of scanned magnetic images of the rivet with and without corrosion. The data have removed the offset by subtracting the first line scan data, as described in Equation (4). The rivet signal has two peaks with high intensity. With large corrosion in Figure 4 (e.g., Ø10 × d0.9), the corrosion signal could be observed clearly. However, when the corrosion size is small, it is hard to recognize the corrosion signal and be buried in the high-intensity signal of the rivet, as observed in Figure 5. The corrosion signal quickly decreases as the depth and diameter decrease.

$$\boldsymbol{V}(i,j) = \boldsymbol{V_{RMS}}(i,j) - \boldsymbol{V_{RMS}}(i,0) \tag{4}$$

where $\boldsymbol{V_{RMS}}(i,j)$ is the root-mean-square voltage of the Hall sensor element i-th at scan index j; $\boldsymbol{V_{RMS}}(i,0)$ is the root-mean-square voltage of the Hall sensor element i-th at the first scan index. This is known as offset voltage, and $\boldsymbol{V}(i,j)$ is the processed voltage after offset subtraction of the sensor i-th at scan index j.

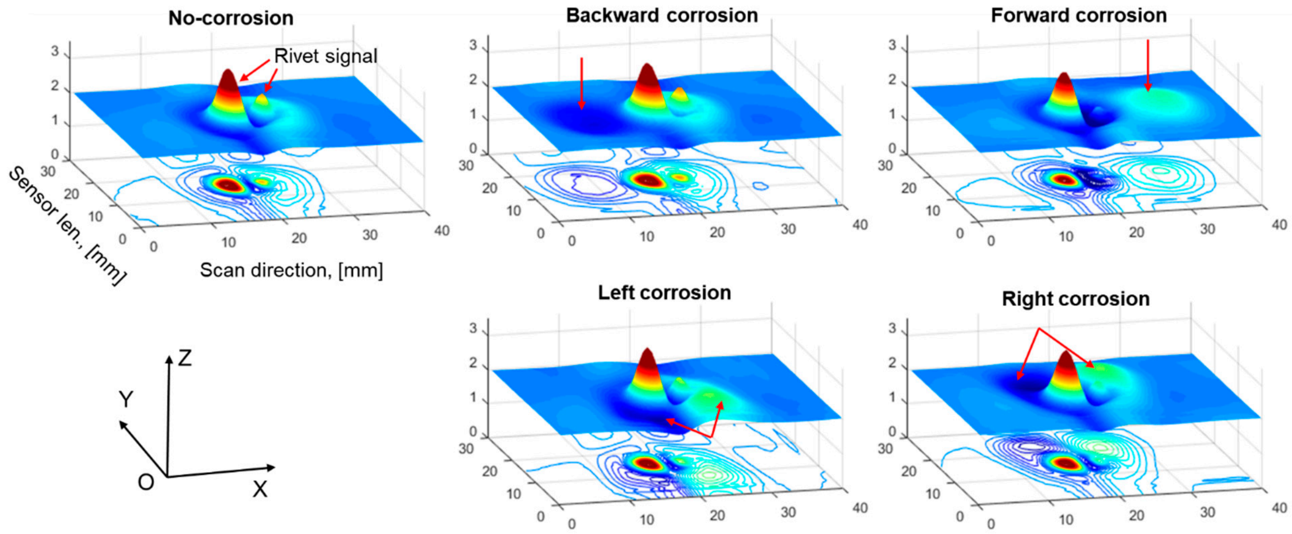

Figure 4. Sample scanned images of five different types of rivets: no corrosion, backward corrosion, forward corrosion, left corrosion, and right corrosion (Ø10 × d0.9).

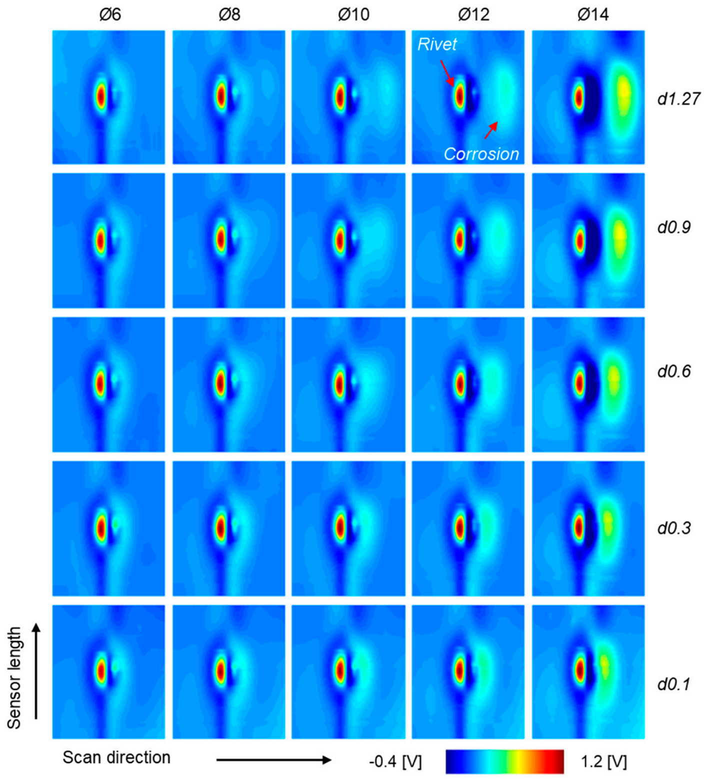

Figure 5. Sample scanned images of 25 rivets with forward corrosion.

One of the big challenges when applying machine learning techniques in electromagnetic testing is the limited amount of data for training the machine-learning models. Thus, we evaluate three training/validation dataset splitting strategies which are "mixing", "increasing", and "shifting", as described in Figure 6. In the "mixing" strategy, the training/validation dataset has a ratio of 80/20 as the normal splitting approach. There is a total of 25 distinguished corrosions: 20 corrosions for training and 5 corrosions for validation. The number of corrosions in the training dataset increases from a low volume to a high volume in the "increasing" strategy. Each increasing step is 20% of the total corrosion with respect to 5 distinguished volumes. There are four increasing steps, which are 20%, 40%, 60%, and 80%, of volumes for training and the remaining for validation. In the "shifting" strategy, the training dataset is fixed with only 20% of the total samples, but the volume is shifted from small to large size $P_{1\sim5}$. The detailed splitting dataset is shown in Table 2.

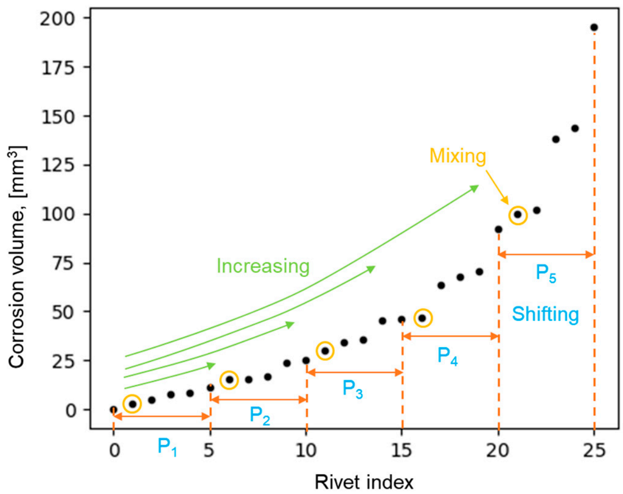

Figure 6. Training/validation dataset split strategies based on corrosion volume to evaluate the performance of machine learning algorithms: selection of corrosion for training dataset with 20% data of the entire volumes (mixing), 20% corrosion shifting from low to high volumes ($P_{i=1:5}$), and increasing volumes from low to high (20~80%).

Table 2. Dataset splitting strategy and its corresponding amount of data and distinguished volumes.

Data Splitting Strategy	Training Dataset (The Remained Data Is in the Validation Dataset)	
	Amount of Data	*Distinguished Volumes*
Mixing	80% of data	5 volumes selected from small to large with a step of 5
Increasing	10%, 20%, 30%, 40%, 50%, 60%, 70%, 80% of data	With respect to 2, 5, 7, 10, 12, 15, 17, 20 volumes increasing from small to large
Shifting	Fixed 20% of data for all shifting ranges	Volume in a range: P1, P2, P3, P4, P5

4. Machine Learning Algorithms

4.1. Principal Component Analysis (PCA)

PCA is a data-driven feature-extraction method. High dimensional data could be efficiently compressed into low dimensional data with less information loss. Our magnetic dataset has a high number of features (e.g., 4480 features) which are the pixels of the magnetic image. Therefore, reducing the number of features before feeding to classification models is necessary. Suppose the dataset has a size of $M \times N$; where M and N are the number of magnetic images and number of features, respectively. The dataset is then normalized to scale the features in a similar range, as described by Equations (5) and (6). The covariance matrix $\boldsymbol{R}$ is computed, as described in Equation (8), and its eigenvalues ($\lambda = diag(\boldsymbol{S})$) and eigenvectors ($\boldsymbol{U}, \boldsymbol{H}$) are obtained by the singular vector decomposition method, as described in Equation (8). The collection of eigenvectors is a new orthogonal space of the data. Thus, the projected data, which is the projection of the normalized data on these eigenvectors, are new feature data, as described in Equation (9). The number of new features is the same as the number of selected eigenvectors selected by eigenvalues. Usually, the eigenvalues are sorted in descent order for easier selection, and the high value of an eigenvalue represents a high value of data. The retained information of data could be estimated by the cumulative explained variance (E), as expressed by Equation (10).

$$\boldsymbol{V_m}(i,j) = \boldsymbol{V}(i,j) - \frac{1}{M}\sum_{j=1}^{M} \boldsymbol{V}(i,j), \tag{5}$$

with $i = 1 : SN, j = 1 : M$.

$$\boldsymbol{V_{norm}}(i,j) = \frac{\boldsymbol{V_m}(i,j)}{\varepsilon + \sqrt{\frac{1}{M}\sum_{j=1}^{M}\boldsymbol{V_m^2}(i,j)}}, \tag{6}$$

with $i = 1 : SN, \;\; j = 1 : M$; ε is a small number to prevent zero division.

$$\boldsymbol{R} = \frac{1}{M}\boldsymbol{V_{norm}^T}\cdot\boldsymbol{V_{norm}} \tag{7}$$

$$\boldsymbol{R} = \boldsymbol{USH}^T \tag{8}$$

$$z_k = \boldsymbol{U}_k^T\boldsymbol{X_{norm}} \tag{9}$$

with k is the k-th features selected by eigenvalue λ_k.

$$E = \frac{\sum_{k=1}^{K}\lambda_k}{\sum_{k=1}^{N}\lambda_k} \qquad \lambda = diag(\boldsymbol{S}). \tag{10}$$

where i and j are the sensor element index and scan index, respectively; $\boldsymbol{V_m}$ is the Hall voltage after mean subtraction; $\boldsymbol{V_{norm}}$ is the normalized Hall voltage; $\boldsymbol{R}$ is the covariance matrix of Hall voltage $\boldsymbol{V_{norm}}$; $\boldsymbol{U}$ and $\boldsymbol{V}$ are left and right eigenvectors, respectively; λ_k is the k-th eigenvalue, $\lambda = diag(\boldsymbol{S})$; z_k is the projection of data on the k-th eigenvector; and $\boldsymbol{E}$ is the cumulative explained variance.

Figure 7 shows the distribution of data on the first three orthogonal vectors (three principal components). Backward and forward corrosions could be distinguished from the others. However, left and right corrosions were mixed with no corrosion. Thus, it requires more components to be used for better classification. This is reasonable because the cumulative explained variance of the three principal components is only about 43%. The cumulative explained variance quickly increases as the number of principal components increases, as observed in Figure 8. The cumulative explained variance approaches 100% with just less than 100 principal components. Thus, the features of the data were significantly reduced (e.g., 4480 to less than 100).

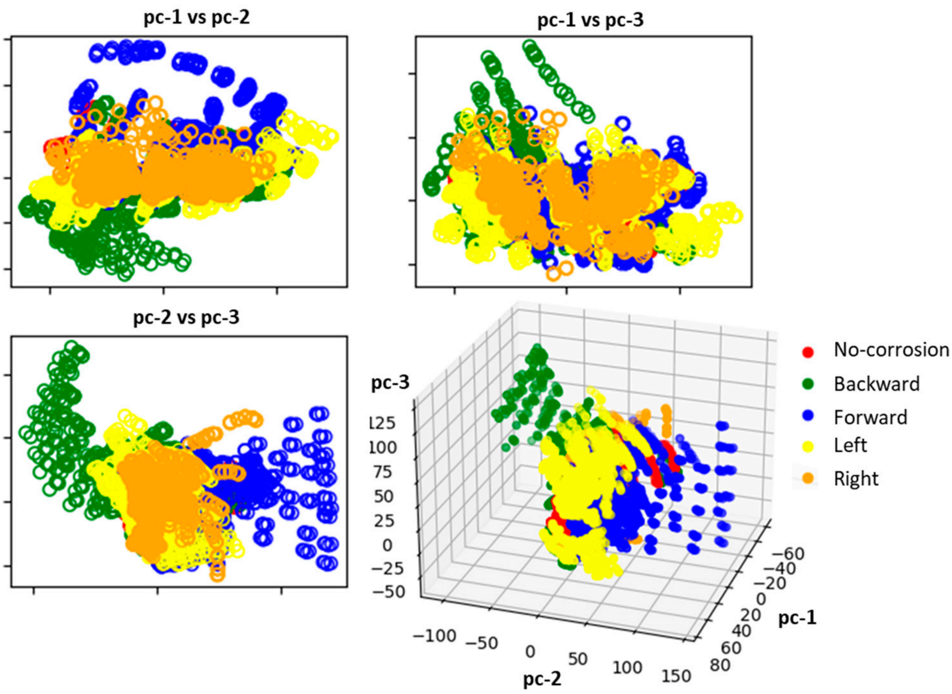

Figure 7. Projection of dataset on three principal components.

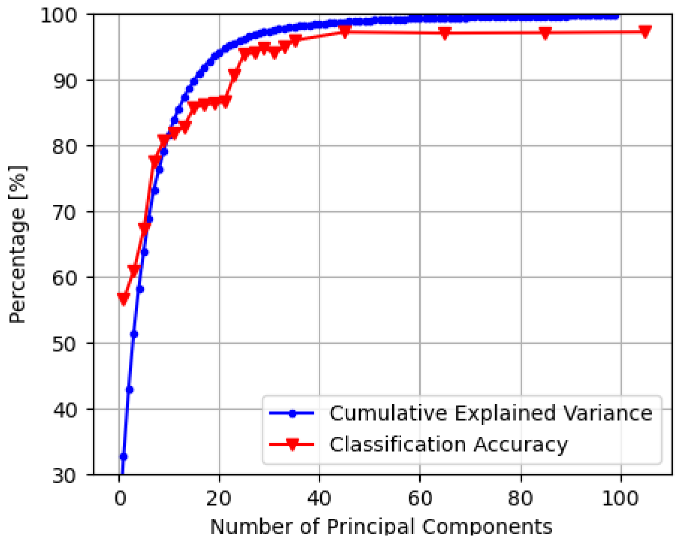

Figure 8. Classification accuracy of SVM model and cumulative explained variance with the number of principal components.

4.2. Support Vector Machine (SVM)

SVM is an efficient learning algorithm being used in classification problems. SVM mapped nonlinear data into a high-dimensional feature space and separated the data by maximizing the hyperplane boundaries. SVM maximizes the gap between data points with hyperplane boundaries, which is the support vectors. SVM originally solved binary classification (classify two classes labeled +1 and −1) and could be extended to multi-classes classification by combining multiple binary classifiers. Thus, this section presents key points of the SVM method for binary classification.

Giving a training dataset $D = \{(x_i, y_i)\}$ with $i = 1, 2, 3, \ldots, m$, $x_i \in R^n$ and $y_i = \pm 1$, our goal is to find a hyperplane parameterized by $\omega \in R^h$ and $b \in R$ such that it correctly separates most of the samples. The hyperplane is formulated by Equation (11), where $g(.)$ is a nonlinear equation mapping the input into a high dimensional space. SVM minimizes the loss function L to maximize the margin between the hyperplanes and data points, as described by Equation (11).

$$h(x) = \omega^T \cdot g(x) + b = 0 \tag{11}$$

$$\begin{gathered} min\left\{L = \frac{1}{2}\omega^T \omega + C\sum_{i=1}^{n} \vartheta_i\right\} \\ \text{subject to}:\ y_i\left(\omega^T \cdot g(x) + b\right) \geq 1 - \vartheta_i,\ \text{with}\ \vartheta_i \geq 0,\ i = 1, 2, \ldots, m \end{gathered} \tag{12}$$

where C is the regulation factor and ϑ_i is imperfection allowed error from the data point i to the hyperplane. To solve the optimization problem, Lagrange multiplier method could be used, which is described by Equation (13); where α and β are the Lagrange multiplier. The decision function is then could be calculated by Equation (13); where $K(x, x_i)$ is the kernel function. Some common kernel functions are linear, polynomial, radial basic function, and multilayer perceptron [19]. To find hyperparameters of C and K, we used the grid search method.

$$\Gamma = L - \sum_{i=1}^{m} \alpha_i (y_i [\omega^T \cdot g(x) + b] - 1 + \vartheta_i) - \sum_{i=1}^{n} \beta_i \vartheta_i \tag{13}$$

$$h(x) = \sum_{i=1}^{m} \alpha_i K(x, x_i) + b \tag{14}$$

Figure 9 shows the validation accuracy of "mixing" datasets using the SVM with the different number of principal components (PCs). The optimum kernel is a linear $K(x, x_i) = x^T x$. As the number of PCs increases from 1 to 45, the classification accuracy quickly increases. The accuracy reaches its maximum at about 97%, with the number of PCs over 45. This is reasonable because the cumulative explained variance E increases as the number of PCs increases. Thus, we could use a few features (99% of E is used in the later results) to train the machine-learning models.

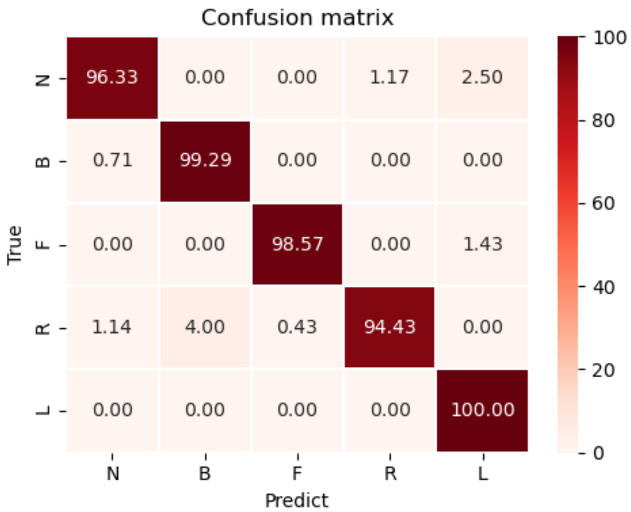

Figure 9. Confusion matrix of the SVM model for five classes with "mixing" dataset: no corrosion (N), backward (B), forward (F), left (L), and right (R).

4.3. Classification Results

Figure 9 shows the confusion matrix of the SVM model with "mixing" validation dataset. The cumulative explained variance E was set at 99% with respect to 53 PCs. The results show a good classification with 96.33%, 99.29%, 98.57%, 94.43%, and 100% for no corrosion, backward, forward, left, and right corrosion. The lowest accuracy is for the left corrosion (94.43%), but the wrong prediction is mostly backward corrosion, which is also corrosion near a location. The average accuracy of the model is 97.17%. Figure 10 shows the probability of the prediction for each type of corrosion of the validation dataset. The probability increases as the corrosion volume increase. The average probability is over 90%, with the volume over 25 mm^3.

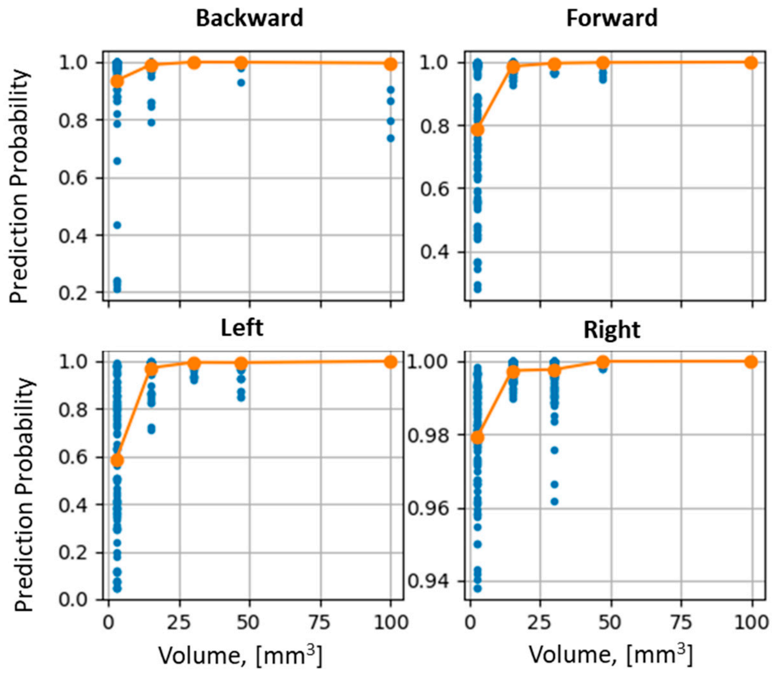

Figure 10. Probability of classification by SVM model with "mixing" dataset.

The SVM model provides good classification accuracy with a large training dataset ratio (80% of the entire dataset). Thus, we will evaluate the model with a smaller training dataset. Datasets "increasing" and "shifting" are used. The "increasing" dataset provides the increasing number of samples in the training dataset from 10% to 80% of the entire dataset, and the "shifting" dataset provides a fixed ratio of 20% of the entire dataset but with a different range of volume from small to large, as described in Table 2. We performed several other machine-learning models, which are Naïve Bayes (NB), K-nearest Neighbor (KNN), Random Forest (RF), and Logistic Regression (LG) classifiers. Figure 11 shows the classification accuracy of the five machine-learning models with the two training datasets. With the increasing number of training datasets from 10% to 40%, the model accuracy quickly increased from 46% to 95%, as shown in Figure 11a. Then, the accuracy slowly increases as the training dataset is larger. The maximum accuracy was about 99%, with a 60–80% ratio of the training dataset using the SVM method. The LG method provides slightly smaller accuracy than the SVM method. The KNN and RF methods provide similar accuracy. The NB method provides the worst performance. While keeping the same ratio of 20% and shifting the volume ranges from small to large in the "shifting" dataset, the accuracy of the machine-learning model increased, peaked at range P_2 (volume in from 15.0 to 25.4 mm^3), and decreased as the volume range increased.

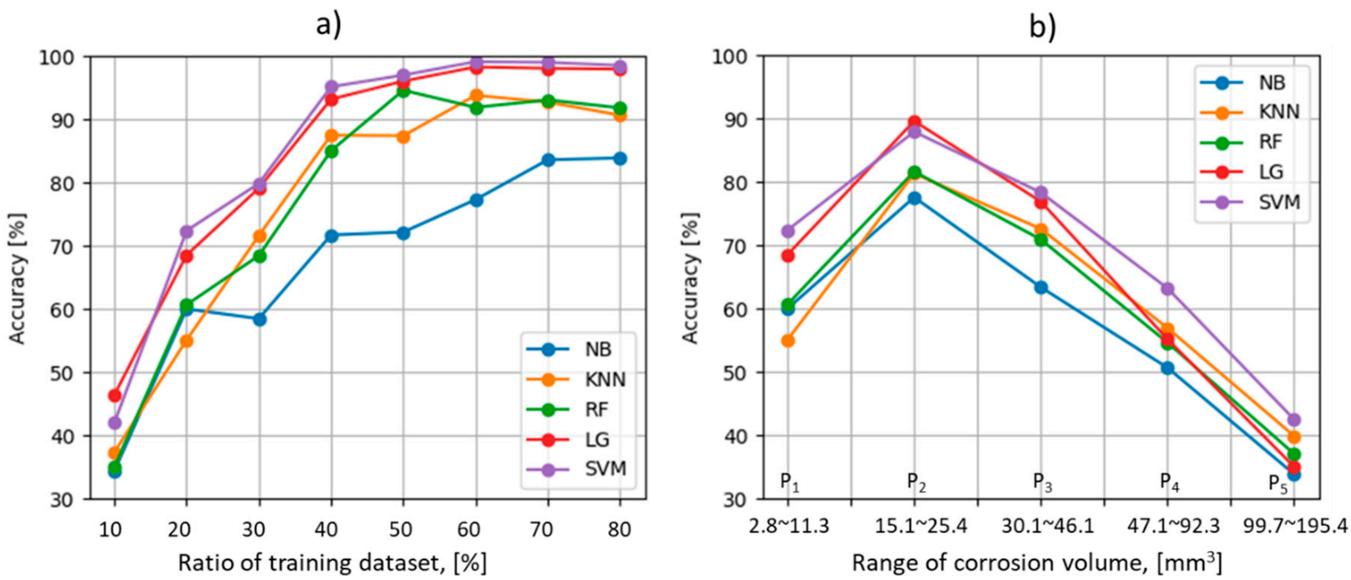

Figure 11. Validation accuracy of different machine-learning models with: (**a**) a different number of training datasets (ratio with entire dataset) in "increasing" dataset and (**b**) fixed 20% ratio at different corrosion volume ranges in "shifting" dataset.

4.4. Probability of Detection

This section shows the probability of detection (POD) of the SVM method. As the results in the previous section show, machine-learning models such as SVM, LG, RF, and KNN show good classification performance in the detection of corrosion and its location. Thus, it is feasible to evaluate the performance of the machine-learning models with a small amount of data and/or small corrosion sizes. Thus, in this section, we only use 20% of the dataset for training the SVM model and with the corrosion volumes in a small range of 15.0 to 25.4 mm^3 (P_2).

Figure 12 shows the classification results of the corrosion using SVM method. The SVM method provides good results on the unseen validation dataset (80% of the total dataset). The average accuracy is 89.48%, with the accuracy of no corrosion, backward, forward, left, and right corrosion being 99.17%, 89.56%, 85.42%, 79.17%, and 91.67%, respectively. The rivets without corrosion are the easiest to detect (99%), and the rivets with corrosion are harder. Among the corrosion, right corrosion is the easiest to detect with 92% accuracy.

The forward corrosion has low accuracy, but its wrongly classified labels were on the left and right corrosion (10%), and only 6% (just after right corrosion with 4%) corrosion was incorrectly classified as no corrosion. The F1 score is a harmonic factor between precision and recall of the classification system. The F1 score is better for evaluating the performance of the model and its results for each class of corrosion, as shown in Figure 12b and Table 3. The F1 score for backward, forward, left, and right corrosion was 89.9%, 91.53%, 86.36%, and 93.62%, respectively. The F1 scores for right and forward corrosion are the highest values, which means that the right and forward corrosion are easier to detect than the other ones. The area under the curve (AUC) of the forward, backward, left, and right corrosion was 98.45%, 96.52%, 98.58%, and 95.88%, respectively, which are high values. The highest value is for the right corrosion. The AUC value tells us that the right corrosion is the easiest to detect by the model.

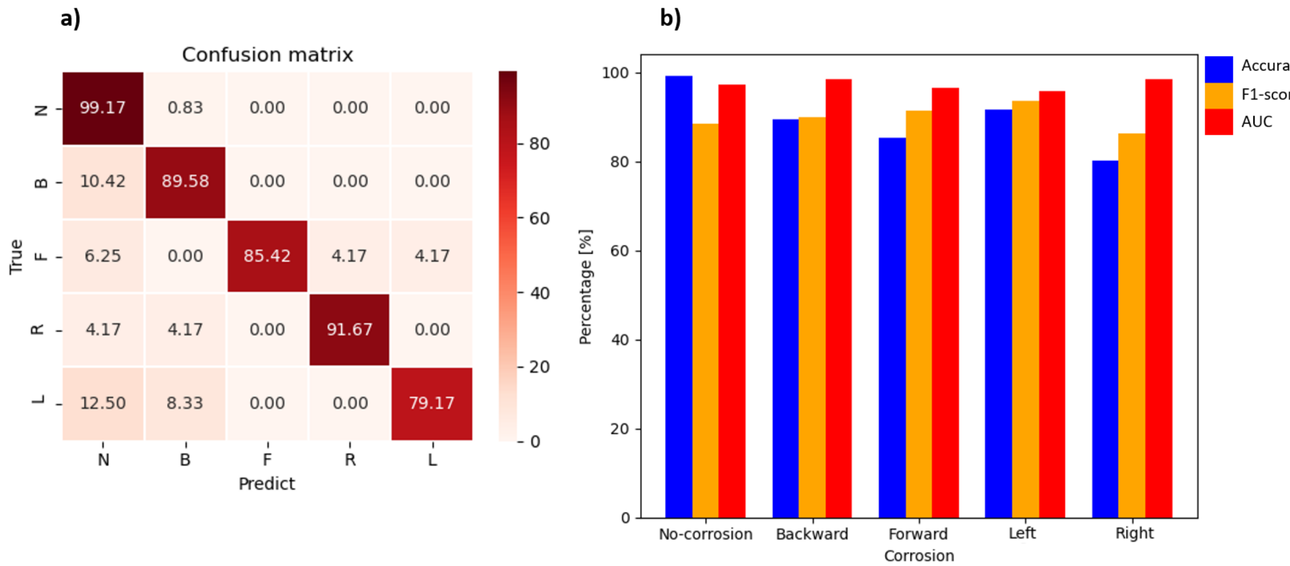

Figure 12. Classification results using 20% data for training at a small volume range (P_2:15.0 to 25.4 mm^3): (**a**) confusion matrix and (**b**) evaluation metrics of accuracy, F1 score, and AUC for each class.

Table 3. Evaluation metrics and comparison of the proposed method with the SoA method [22].

Corrosion	SoA Method [22]			SVM Using 20% Data for Training		
	Accuracy	F1 Score	AUC	Accuracy	F1 Score	AUC
Backward	60.0	89.58	89.58	89.58	89.90	98.45
Forward	56.0	85.42	85.42	85.42	91.53	96.52
Right	**64.0**	**91.67**	**91.67**	**91.67**	**93.62**	**98.58**
Left	61.0	80.21	80.21	80.21	86.36	95.88

The comparison of the classification accuracy, F1 score, and AUC of the SVM method with the previous study using "sum of area" feature (SoA) [22] is shown in Table 3. The SVM method significantly improves the classification results, which are 26.47%, 3.3%, and 10.64% of the accuracy, F1 score, and AUC, respectively. The ROC of the SVM and the SoA feature method are shown in Figure 13. It is observed that the SVM provides significant results compared to the SoA feature method.

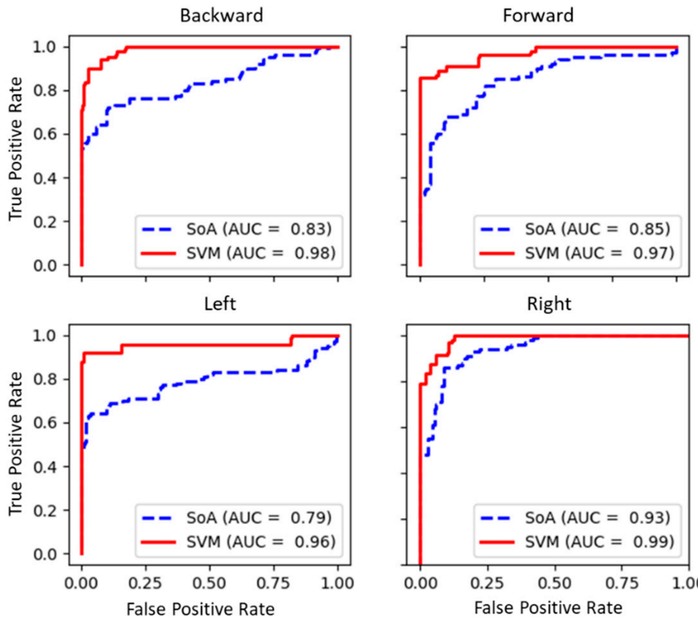

Figure 13. Receiver operating characteristic (ROC) of the SVM method and the SoA method. The SVM model uses 20% data for training at a small volume range (P_2:15.0 to 25.4 mm^3).

Figure 14 shows the POD curves of the SVM method compared to the SoA feature method. The parameters of the POD curves were calculated by mh1823 POD software V4.0.1 developed by Charles Annis [26] based on the MIL-HDBK methodology. The POD calculation was based on hit–miss data (hit = "1", miss = "0") using the logit model. The POD curves show that the SVM method is better than the SoA feature method, which increases the POD of small corrosion size. The corrosion with a volume of 48.08, 24.85, 63.16, and 41.53 mm^3 for forward, backward, left, and right corrosion could be detected with a 90% POD and 95% confidence boundary ($a_{90/95}$), while those corrosion volumes were 96.24, 83.41, 101.90, 46.36 mm^3 for forward, backward, left, and right corrosion, respectively. The detailed POD characters are shown in Table 4. It is noted that the SVM model was trained with only 20% of the corrosion at a small volume range (15.0 to 25.4 mm^3).

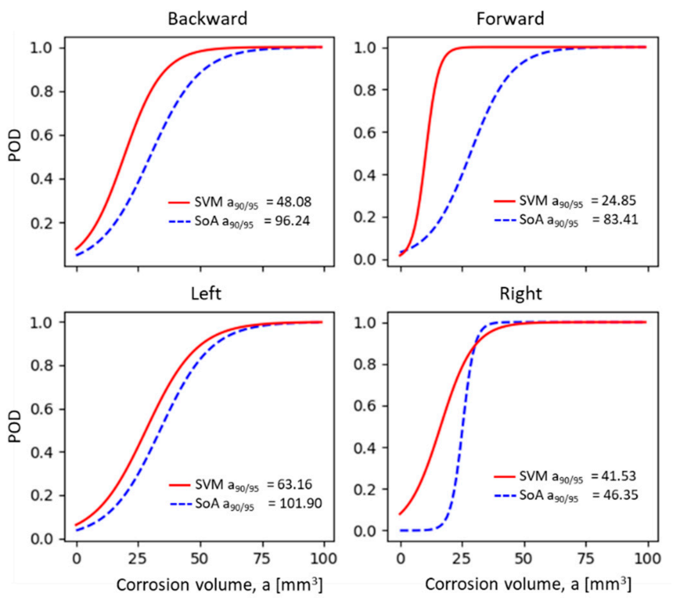

Figure 14. POD curves comparison between SVM and SoA method [22]. SVM model used only 20% of the data for training at a small volume range (P_2:15.0 to 25.4 mm^3).

Table 4. Probability of detection results.

Corrosion	SoA Method [22]		SVM Using 20% Data for Training	
	a_{90}	$a_{90/95}$	a_{90}	$a_{90/95}$
Backward	51.91	96.24	36.55	48.08
Forward	46.65	83.41	**16.02**	**24.85**
Right	30.53	46.35	**31.08**	**41.53**
Left	56.55	101.90	50.92	63.16

5. Conclusions

This paper proposes a detection of hidden corrosion at the riveting site in a multilayer structure method using electromagnetic testing and machine learning. The electromagnetic testing system uses a Hall sensor array for measuring the distribution of the electromagnetic field of the rivet and hidden corrosion in a multilayer structure. Machine learning algorithms were used to enhance the detectability of the hidden corrosion. PCA was used to auto-extract features of electromagnetic signal; e.g., it significantly reduces the number of features from 4480 to 53 while keeping 99% of the signal information. Then, machine learning classifiers such as SVM, LG, RF, KNN, and Naïve Bayes were used to detect both the presence of the hidden corrosion and its location around the rivet (forward, backward, left, and right position). Among the classifiers, SVM shows the best performance, which provides an accuracy of about 99% with 60–80% data for training.

The SVM method was also evaluated with a smaller amount of data for training (e.g., only 20%) at small sizes of corrosion (e.g., 15.0 to 25.4 mm^3 volume). The SVM method provides an 89.48% average accuracy, which is over 26.47% compared to the previous SoA feature method. Among the different locations of corrosion, the right corrosion is the easiest to detect (91.67% of accuracy). In addition, the POD of the system was also improved using the SVM method. The system could detect backward, forward, left, and right corrosion with a POD of 90% and confidence of 95% ($a_{90/95}$) for a volume of 48.08, 24.85, 41.53, 63.16 mm^3, respectively. The results also suggest that we should train the machine-learning model with small corrosions rather than training with large corrosions. Once the model is trained well with small corrosions, it will be easy to detect large corrosion. However, it should not be so small that the model could be underfitting since it is hard to detect very small corrosion.

Author Contributions: Conceptualization, J.L.; Data curation, V.S.L. and D.-K.L.; Formal analysis, M.L.; Funding acquisition, J.L.; Methodology, J.L.; Project administration, J.L.; Resources, V.S.L., D.K.N., D.-K.L. and J.L.; Software, M.L. and D.K.N.; Supervision, M.L.; Validation, V.S.L., D.K.N. and D.-K.L.; Visualization, M.L., V.S.L. and D.K.N.; Writing—original draft, M.L.; Writing—review & editing, J.L. All authors have read and agreed to the published version of the manuscript.

Funding: This study was supported by research fund from Chosun University, 2020.

Conflicts of Interest: The authors declare no conflict of interest.

References

1. Czaban, M. Aircraft Corrosion—Review of Corrosion Processes and its Effects in Selected Cases. *Fatigue Aircr. Struct.* **2018**, *2018*, 5–20. [CrossRef]
2. Hendricks, W.R. The Aloha-airlines accident—A new era for aging aircraft. In *Structural Integrity of Aging Airplanes*; Atluri, S.N., Sampath, S.G., Tong, P., Eds.; Springer: Berlin/Heidelberg, Germany, 1991; pp. 153–165.
3. Pitt, S.; Jones, R. Multiple-site and widespread fatigue damage in ageing aircraft. *Eng. Fail. Anal.* **1997**, *4*, 237–257. [CrossRef]
4. Xufei, G.; Yan, H. Ultrasonic Total Focusing Imaging Method of Multilayer Composite Structures Using the Root-Mean-Square (RMS) Velocity. *Adv. Mater. Sci. Eng.* **2021**, *2021*, 2745732.
5. Ruikun, W.; Hong, Z.; Ruizhen, Y.; Wenhui, C.; Guotai, C. Nondestructive Testing for Corrosion Evaluation of Metal under Coating. *Adv. Mater. Sci. Eng.* **2021**, *2021*, 6640406.
6. Kuts, Y.V.; Yeremenko, V.S.; Monchenko, E.V.; Protasov, A.G. Ultrasound method of multilayer material thickness measurement. *AIP Conf. Proc.* **2009**, *1096*, 1115–1120. [CrossRef]

7. Fitzpatrick, G.; Thome, D.; Skaugset, R.; Shih, E.; Shih, W. Magneto-optical/ Eddy current imaging of aging aircraft—A New NDI Technique. *Mater. Eval.* **1993**, *51*, 1402–1407.
8. Thome, D.K.; Fitzpatrick, G.L.; Skaugset, R.L.; Shih, W.C.L. Aircraft corrosion and defect inspection using advanced magneto-optic imaging technology. *Proc. SPIE* **1996**, *2945*, 365–373.
9. Sasi, B.; Rao, B.P.C.; Jayakumar, T.; Raj, B. Development of Eddy Current Test Procedure for Non-destructive Detection of Fatigue Cracks and Corrosion in Rivets of Air-intake Structures. *Def. Sci. J.* **2009**, *59*, 106–112. [CrossRef]
10. Karpenko, O.; Efremov, A.; Ye, C.; Udpa, L. Multi-frequency fusion algorithm for detection of defects under fasteners with EC-GMR probe data. *NDT E Int.* **2020**, *110*, 102227. [CrossRef]
11. Chady, T.; Okarma, K.; Mikołajczyk, R.; Dziendzikowski, M.; Synaszko, P.; Dragan, K. Extended Damage Detection and Identification in Aircraft Structure Based on Multifrequency Eddy Current Method and Mutual Image Similarity Assessment. *Materials* **2021**, *14*, 4452. [CrossRef]
12. Sophian, A.; Gui, Y.T.; Taylor, D.; Rudlin, J. A feature extraction technique based on principal component analysis for pulsed Eddy current NDT. *NDT E Int.* **2003**, *36*, 37–41. [CrossRef]
13. Abidin, I.Z.; Mandache, C.; Tian, G.Y.; Morozov, M. Pulsed eddy current testing with variable duty cycle on rivet joints. *NDT E Int.* **2009**, *42*, 599–605. [CrossRef]
14. Kim, J.; Yang, G.; Udpa, L.; Udpa, S. Classification of pulsed eddy current GMR data on aircraft structures. *NDT E Int.* **2010**, *43*, 141–144. [CrossRef]
15. Horan, P.; Lowerhill, P.R.; Krause, T.W. Pulsed eddy current detection of defects in F/A-18 inner wing spar without wing skin removal using modified principal component analysis. *NDT E Int.* **2013**, *44*, 21–27. [CrossRef]
16. Stott, C.A.; Underhill, P.R.; Babbar, V.K.; Krause, T.W. Pulsed Eddy Current Detection of Cracks in Multilayer Aluminum Lap Joints. *Sens. J. IEEE* **2015**, *15*, 956–962. [CrossRef]
17. Postolacheab, O.; Ribeiroac, A.L.; Ramos, H.G. GMR array uniform eddy current probe for defect detection in conductive specimens. *Measurement* **2013**, *46*, 4369–4378. [CrossRef]
18. Tianyu, D.; Zhaohe, Y.; Hua, H.; Pingjie, H.; Dibo, H.; Guangxin, Z. A method for characterizing defects in multilayer conductive structures by combining pulsed eddy current signals with PCA components. *AIP Conf. Proc.* **2019**, *2102*, 80003. [CrossRef]
19. Fu, X.; Zhang, C.; Peng, X.; Jian, L.; Liu, Z. Towards end-to-end pulsed eddy current classification and regression with CNN. In Proceedings of the IEEE International Instrumentation and Measurement Technology Conference (I2MTC), Auckland, New Zealand, 20–23 May 2019; pp. 1–5.
20. Huang, P.; Luo, X.; Hou, D.; Yang, Z.; Zhao, L.; Zhang, G. Lift-off nulling and internal state inspection of multilayer conductive structures by combined signal features in pulsed eddy current testing. *Nondestruct. Test. Eval.* **2018**, *33*, 272–279. [CrossRef]
21. Le, M.; Kim, J.; Kim, S.; Wang, D.; Hwang, Y.; Lee, J. Nondestructive Evaluation Algorithm of Fatigue Cracks and Far-side Corrosion around a Rivet Fastener in Multi-layered Structures. *J. Mech. Sci. Technol.* **2016**, *30*, 4205–4215. [CrossRef]
22. Kim, J.; Le, M.; Lee, J.; Kim, S.; Hwang, Y. Nondestructive evaluation of far-side corrosion around a rivet in a multilayer structure. *RNDE* **2016**, *29*, 1–20. [CrossRef]
23. Chollet, N.S.; Solignac, A.; Lecoeur, M.P.; Fermon, C. MR sensors arrays for eddy current testing. In Proceedings of the 11th International Symposium on NDT in Aerospace (AeroNDT 2019), Paris-Saclay, France, 13–15 November 2019.
24. Aldrin, J.C.; Motes, D.; Forsyth, D.S. Enhanced image processing methods for GMR array inspections of multilayer metallic structures. *AIP Conf. Proc.* **2013**, *1511*, 699–706. [CrossRef]
25. Cristianini, N.; Shawe-Taylor, J. *An Introduction to Support Vector Machines and Other Kernel-Based Learning Methods*; Cambridge University Press: Cambridge, UK, 2000. [CrossRef]
26. Annis, C. R Package mh1823, Version 4.0.1. Available online: https://statistical-engineering.com/mh1823/ (accessed on 15 February 2022).